

## Article

# Optimization Design of a Pneumatic Wheat-Shooting Device Based on Numerical Simulation and Field Test in Rice–Wheat Rotation Areas

Chao Wang , Hongwen Li, Jin He , Qingjie Wang, Caiyun Lu and Hanyu Yang

College of Engineering, China Agricultural University, Beijing 100083, China; superc@cau.edu.cn (C.W.); lhwen@cau.edu.cn (H.L.); wangqingjie@cau.edu.cn (Q.W.); lucaiyun@cau.edu.cn (C.L.); yanghanyu@cau.edu.cn (H.Y.)

\* Correspondence: hejin@cau.edu.cn; Tel.: +86-10-62-737-300

**Abstract:** In rice–wheat rotation areas of China, traditional wheat seeders have severe blockage, low working efficiency and poor seeding quality. In this study, a pneumatic shooting technology was designed, consisting mainly of a nozzle, shell and acceleration tube. To improve the sowing depth of the pneumatic shooting device, the response-surface methodology of structure parameters and CFD simulation technology was adopted in this work. The effects of working pressure, acceleration-tube diameter and throat distance on the steady airflow length (SAL) and steady airflow velocity (SAV) were studied by airflow field analysis, and the response-surface method was introduced to obtain the optimal parameter combination of the pneumatic shooting device for wheat. The optimal parameter combination was working pressure 686 kPa, acceleration tube diameter 8 mm and throat distance 20 mm. The simulation result showed that the optimized device of pneumatic shooting performs faster and has more stable airflow field characteristics in comparison to the initial device. The field test demonstrated that the optimized device has about 68% higher seeding depth than the initial device. The average field-seeding depth of the optimized device was 19.95 mm, which is about 68% higher than the initial device. The emergence rate for the optimized device was about 88.7% without obvious reduction. CFD and response-surface methods positively affect the optimization of pneumatic wheat-shooting devices, and the significance was also confirmed.

**Keywords:** wheat; pneumatic shooting; simulation; response surface experiment; airflow field



**Citation:** Wang, C.; Li, H.; He, J.; Wang, Q.; Lu, C.; Yang, H. Optimization Design of a Pneumatic Wheat-Shooting Device Based on Numerical Simulation and Field Test in Rice–Wheat Rotation Areas.

*Agriculture* **2022**, *12*, 56.

<https://doi.org/10.3390/agriculture12010056>

agriculture12010056

Academic Editor: John M. Fielke

Received: 3 December 2021

Accepted: 31 December 2021

Published: 2 January 2022

**Publisher's Note:** MDPI stays neutral with regard to jurisdictional claims in published maps and institutional affiliations.



**Copyright:** © 2022 by the authors. Licensee MDPI, Basel, Switzerland. This article is an open access article distributed under the terms and conditions of the Creative Commons Attribution (CC BY) license (<https://creativecommons.org/licenses/by/4.0/>).

## 1. Introduction

As one of the three major grain crops in China, wheat plays a vital role in ensuring national food security. According to the National Bureau of Statistics data, wheat yield in China will be 131.68 million tons in 2020 [1], accounting for about 17% of the world wheat production. Rice–wheat rotation areas located in the Yangtze River Basin are reported as the primary grain-production bases in China, accounting for more than 37% of total wheat-planting areas [2]. Due to the sticky clay soil texture and serious wet damage of the fields in this area, there is a severe blockage, low working efficiency and poor seeding quality for the existing rice-stubble wheat seeders [3–6]. Therefore, it is essential to innovate mechanized sowing technology and improve wheat-sowing quality in rice–wheat rotation areas.

Different from traditional seeding equipment, wheat-shooting technology is not in direct contact with the soil [7]. It has the advantages of no adhesion and blockage, minor soil disturbance and high operation efficiency [8,9]. Wheat-shooting technology includes two types: mechanical shooting and pneumatic shooting. Because of accurate operation and good acceleration effect, the pneumatic wheat-shooting technology is more suitable for wheat sowing in rice-stubble fields. Current research mainly focuses on the wheat soil-ripping parameters of pneumatic wheat shooting under different conditions [10], but there is little study on the internal airflow field analysis and performance improvement of

it. As a reliable flow-field-analysis technology, computational fluid dynamics (CFD) has a wide application in the design and research of wheat seeding [11–13]. Zhao Xiaoshun et al. developed a vacuum-precision, seed-metering device for wheat to improve seed-metering uniformity [14]. With the pressure and velocity simulation of the air chamber by CFD, the structural parameters of the seed-metering device were optimized. And tests showed that the seeding qualified rate of seedlings was 86.66%, and the unqualified rate of seedlings was 5.09%, which meets wheat-precision drilling requirements. Liu Junxiao et al. analyzed the pneumatic loss caused by narrow, long characteristics, and bending of the pinhole-tube wheat uniform-seeding mechanism [15]. The Fluent software was applied to study the airflow pressure variation of different parameter combinations under the orthogonal simulation test, and the principle and types of pneumatic loss were clarified. Test results proved the reliability of the numerical analysis. With the assistance of the fluid-dynamics software, Cheng Xiupei et al. simulated the impacts of different diameters of suction holes on the airflow field of the precision seed-metering device for wheat and thereby produced the optimal diameter parameters of suction holes ranging from 1.4 mm to 1.8 mm [16].

Improving the sowing depth of the pneumatic shooting device is important to ensure wheat-sowing quality. In this paper, CFD is used to study the airflow field of the pneumatic wheat-shooting device (PWSD), aiming at improving acceleration performance. For this purpose, much work was carried out by the kinematic and simulation analysis for the response-surface optimization experiment. We established simulation models based on kinematic analysis of the pneumatic shooting process and acquired the best parameters' combination via the response-surface experiment. Finally, field-test verification of the optimized PWSD was conducted.

## 2. Materials and Methods

### 2.1. Structure and Working Principle of the PWSD

Figure 1a displays the overall structure of the PWSD [17], and the device is mainly composed of nozzle, shell and acceleration tube. The nozzle and acceleration tube were arranged on the interior and bottom of the shell, respectively.

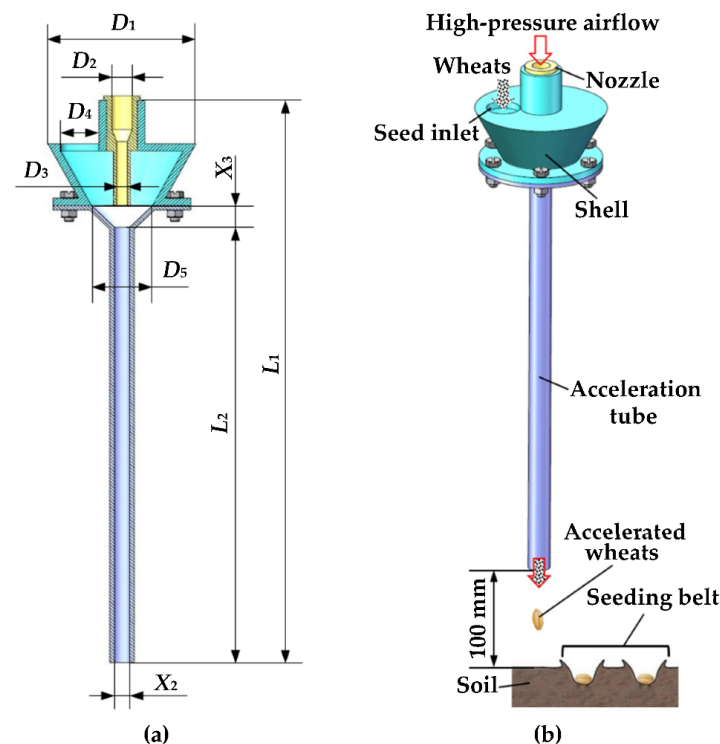


Figure 1. (a) Structure of the PWSD. (b) Pneumatic shooting principle.

The pneumatic wheat-shooting principle is shown in Figure 1b. Before sowing, the ground distance from the bottom of the acceleration tube to the soil surface is 100 mm. After the high-pressure airflow enters the pneumatic wheat-shooting device, a supersonic jet-flow field is formed in its internal cavity. Firstly, the high-pressure airflow enters the nozzle and is compressed to form a compressed airflow. The compressed airflow is ejected from the nozzle to form a jet flow after that. Then the jet flow enters the acceleration tube to develop a positive-pressure acceleration zone. Meanwhile, a vacuum-pressure zone is produced in the shell. Wheat is inhaled into the shell under the entrainment of the vacuum-pressure zone [18,19], and then it is continuously accelerated under the action of the positive-pressure acceleration zone in the acceleration tube. Finally, the wheat with high kinetic energy is shot out from the acceleration tube and is lodged into the soil to complete wheat seeding. With the forward thrust of the seeder, a sowing belt composed of single wheat-seed holes is formed in the soil. Table 1 displays the geometric information of the PWSD.

**Table 1.** Geometric information of the PWSD.

Parameter	Definition	Value (mm)
$D_1$	Shell width	96
$D_2$	Nozzle inlet diameter	13
$D_3$	Nozzle outlet diameter	6
$D_4$	Seed inlet diameter	12.5
$D_5$	Cone diameter	40
$X_2$	Acceleration tube diameter	10
$X_3$	Throat length	10
$L_1$	Total length	390
$L_2$	Acceleration tube length	300

## 2.2. Optimization of PWSD Based on Airflow Simulation

To improve the performance of the PWSD, both a computational analysis and an optimization experimental study were carried out [20,21]. The optimization experiment was designed by a response-surface method, and the internal airflow-field characteristics were acquired by CFD.

### 2.2.1. Experimental Design

The response-surface optimization experiment of the three factors and three levels, based on the single-factor test results [22], was conducted by Box-Behnken central composite design [23–25]. The influence of the working pressure  $X_1$ , the acceleration tube diameter  $X_2$  and the throat distance  $X_3$  on SAV  $Y_1$  and SAL (length of the region with steady airflow velocity)  $Y_2$  were analyzed under the different parameter combinations. There were 17 experimental groups in the response-surface experiment scheme. After the experiment, the velocity curve of the central airflow field of the PWSD was extracted, followed by two kinds of analysis: multiple regression fitting analysis and variance analysis. The optimal combination parameters of the PWSD were predicted. The coding of factor levels is shown in Table 2.

**Table 2.** Factor level coding.

Levels	Factors		
	$X_1$ (kPa)	$X_2$ (mm)	$X_3$ (mm)
−1	300	8	10
0	500	10	15
1	700	12	20

### 2.2.2. Construction of Simulation Model Grid Model

The grid features and extraction of the computational domain are crucial and determine the results of the flow-field analysis [26,27]. SolidWorks 2016 software was adopted to construct the various three-dimensional PWSD models. Then the internal cavity was extracted as the computational domain using SpaceClaim 18.2 software, as shown in Figure 2a. The pressure inlet boundary was given on inlet 1 based on the working pressure of the experiment design scheme, and on inlet 2 with the relative pressure value of 0 kPa. The pressure outlet boundary was given on outlet 1 with the relative pressure value of 0 kPa. All the walls were no-slip wall boundaries. CFD cells of computational domain meshed by Fluent 18.2 software were employed as shown in Figure 2b. According to the structure size of the computational domain in globally scoped sizing, the minimum element size and the maximum element size of the mesh models were 0.2 mm and 30 mm, respectively. The growth rate was 1.2, and the grid type was polyhedral mesh. In addition, curvature function was selected for object faces, and edges and the normal angle was set at 15°; cells per gap was set at 10 in proximity for the edge zone to increase local mesh density, which is because the gas expansion at the nozzle outlet leads to drastic changes in the airflow velocity [28,29]. According to the wall function requirement of the turbulence model, five boundary layers were set near the wall. Statistical data pointed out that the maximum aspect ratio, the  $y^+$ , and the minimum orthogonal quality of all simulation models were controlled in the range of 19–27, 30–280, and 0.5–0.62, respectively.

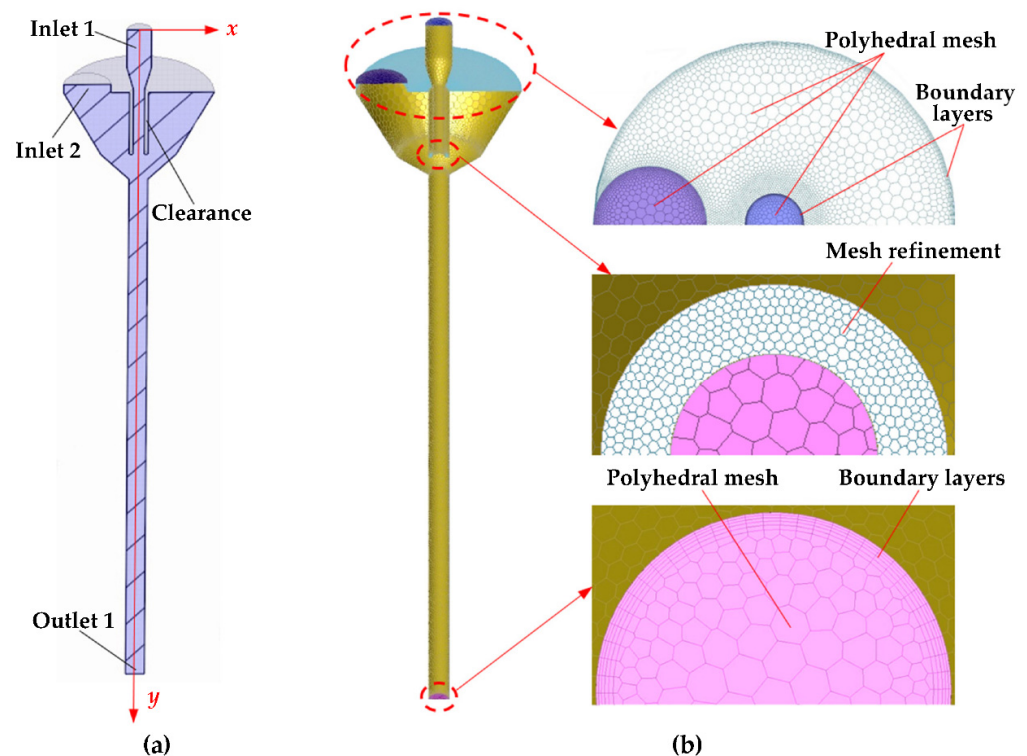


**Figure 2.** (a) Computational region of the PWSD. (b) Grids of the computational region.

### Computational Model

Due to the supersonic speed of airflow in the PWSD, this study defined the airflow as a continuous compressible phase. The following three equations expressed the basic control equations in the CFD simulations represented by the mass and momentum conservation equation and the energy equation [30]:

$$\frac{\partial(\rho u_i)}{\partial x_i} = 0 \quad (1)$$

$$\frac{\partial p}{\partial x_i} = \frac{\mu}{3} \frac{\partial}{\partial x_i} \left( \frac{\partial u_k}{\partial x_k} \right) + \mu \frac{\partial^2 u_i}{\partial x_j \partial x_j} + \rho F_i \tag{2}$$

$$\frac{\partial(\rho E + pu_i)}{\partial x_i} = \frac{\partial(u_j \tau_{ij})}{\partial x_i} - \frac{\partial q_i}{\partial x_i} \tag{3}$$

where  $x_i, x_j,$  and  $x_k$  are the components of Cartesian coordinates;  $u_i, u_j,$  and  $u_k$  are the mean airflow-velocity components;  $\tau_{ij}$  is the stress tensor of airflow;  $\rho$  is the density of airflow;  $q_i$  is the heat flux;  $\mu$  is the viscosity of airflow;  $p$  is the mean airflow pressure;  $F_i$  is the body-force of airflow;  $E$  is the total airflow energy.

Taking the jet-flow characteristics of narrow and long pipes into consideration, the RNG  $k-\epsilon$  model was used in this study. The follow two equations displayed the turbulent kinetic energy and turbulent dissipation:

$$\frac{\partial(\rho k)}{\partial t} + u_i \frac{\partial(\rho k)}{\partial x_i} = \frac{\partial}{\partial x_j} \left( \alpha_k u_c \frac{\partial k}{\partial x_j} \right) + G_v - \rho \epsilon \tag{4}$$

$$\frac{\partial(\rho \epsilon)}{\partial t} + u_i \frac{\partial(\rho \epsilon)}{\partial x_i} = \frac{C_{1\epsilon} \epsilon}{k} G_v - C_{2\epsilon} \frac{\rho \epsilon^2}{k} + \frac{\partial}{\partial x_j} \left( \alpha_\epsilon u_c \frac{\partial \epsilon}{\partial x_j} \right) \tag{5}$$

where  $k$  is the turbulent kinetic energy;  $\epsilon$  is the turbulent dissipation rate;  $\mu_c$  is the equivalent coefficient;  $\alpha_k$  and  $\alpha_\epsilon$  are the airflow Prandtl numbers;  $G_v$  is the velocity gradient;  $C_{1\epsilon}$  and  $C_{2\epsilon}$  are the empirical constants.

The SIMPLE algorithm was adopted to access the pressure–velocity coupling in the simulation [31]. The turbulent kinetic energy was solved by using the second order upwind and finally to improve the computational accuracy. The simulation converges after the RMS residual were less than  $1 \times 10^{-4}$  and airflow velocity of inlet 1 reached steady state.

### 3. Results and Analysis

Table 3 presents the response-surface experiment combinations and results.

**Table 3.** Experiment combinations and results.

No.	X <sub>1</sub> (kPa)	X <sub>2</sub> (mm)	X <sub>3</sub> (mm)	Response Values	
				Y <sub>1</sub> (m·s <sup>-1</sup> )	Y <sub>2</sub> (mm)
1	0	0	0	517	172
2	−1	0	−1	416	184
3	1	1	0	536	149
4	0	−1	1	581	196
5	0	−1	−1	583	182
6	1	0	−1	633	173
7	−1	−1	0	461	198
8	0	0	0	516	177
9	1	0	1	614	162
10	0	0	0	518	169
11	−1	0	1	394	178
12	0	1	−1	520	176
13	−1	1	0	367	161
14	0	0	0	533	180
15	1	−1	0	718	183
16	0	1	1	422	152
17	0	0	0	524	186

Figure 3 shows the velocity variation regularity of the central airflow field ( $y$ -axis) for each group after simulation.

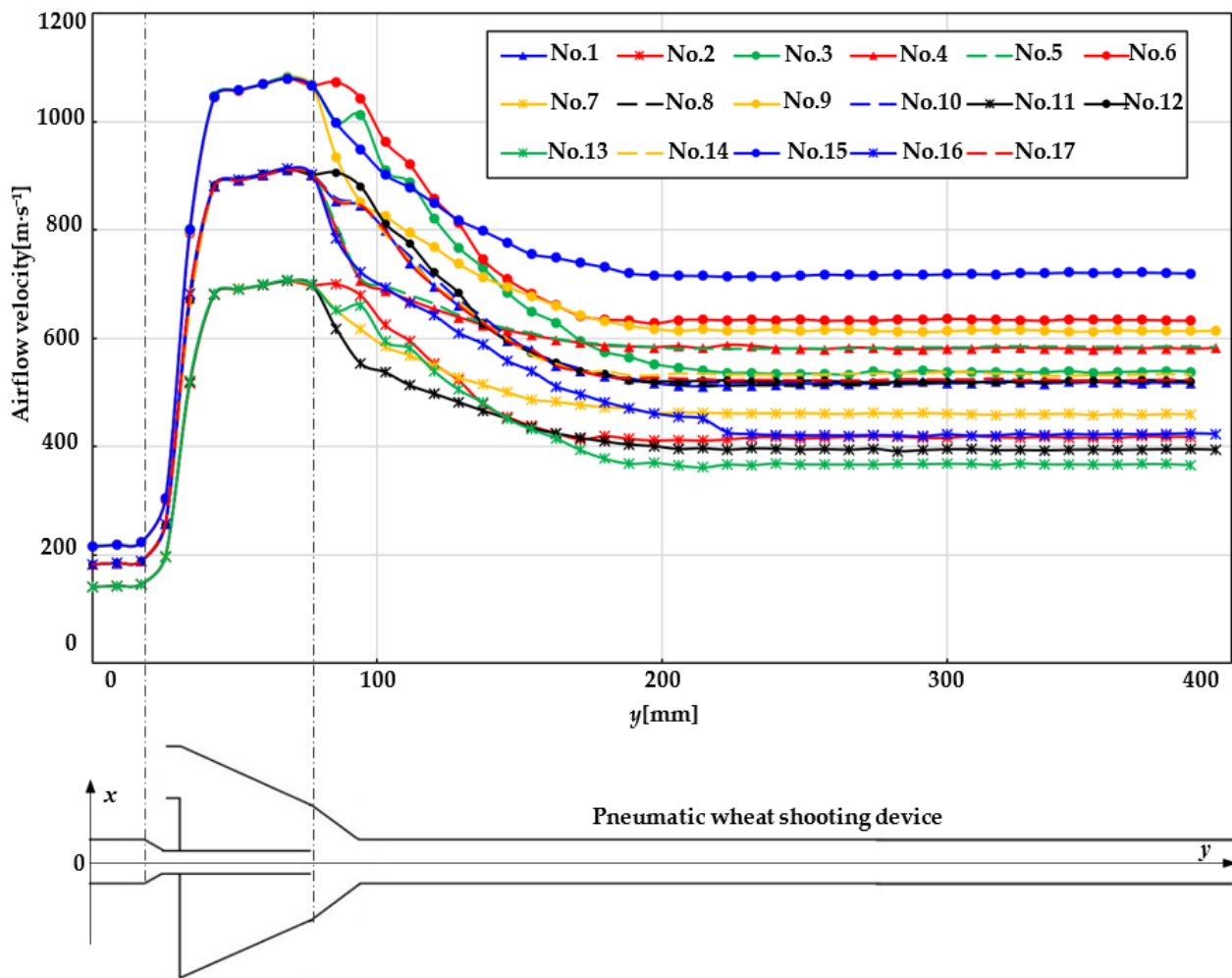


Figure 3. Velocity curve of central airflow field.

Overall, the central airflow velocity showed a sharp increase to a maximum value when  $y$  was 23–75 mm, because the high-pressure airflow was compressed [32] as it passed through the nozzle. The airflow velocity presented a gradual decrease trend in the  $y$  range of 75–220 mm, and the reason is that the airflow was ejected from the nozzle to produce an air-expansion effect [33]. Finally, the airflow velocity remained relatively constant in the acceleration tube. The steady airflow velocity was between the maximum airflow velocity and the high-pressure airflow velocity for each experiment. The higher the high-pressure airflow velocity, the greater the maximum airflow velocity. Table 3 lists the response values of  $Y_1$  and  $Y_2$  that were measured based on Figure 3, and the interaction law between  $Y_1$ ,  $Y_2$  and  $X_1$ ,  $X_2$ ,  $X_3$  was analyzed.

### 3.1. Regression Model Construction

The two-factor interactive (2FI) regression model presenting the interactive influences of  $X_1$ ,  $X_2$ ,  $X_3$  on  $Y_1$ ,  $Y_2$  was established based on Table 3. The regression equations are expressed as:

$$Y_1 = 520.76 + 107.87X_1 - 62.25X_2 - 17.63X_3 - 22X_1X_2 + 0.75X_1X_3 - 24X_2X_3 \quad (6)$$

$$Y_2 = 175.18 - 6.75X_1 - 15.13X_2 - 3.38X_3 + 0.75X_1X_2 - 1.25X_1X_3 - 9.5X_2X_3 \quad (7)$$

Table 4 reveals the variance analysis of the regression equations. There was a highly significant level ( $p < 0.001$ ) for the 2FI regression model of  $Y_1$ ,  $Y_2$ . The significant level ( $p > 0.05$ ) of the lack of fit for all 2FI regression models implies a relatively good fitting

degree in the range of the experimental parameters. Therefore, by using the 2FI regression model of  $Y_1$  and  $Y_2$ , the working and structural parameters of the PWSD can be analyzed and predicted.

**Table 4.** Variance analysis of 2FI regression equation.

Source	$Y_1$ (m·s <sup>-1</sup> )				$Y_2$ (mm)			
	Sum of Squares	Freedom	F Value	Significant Level $p$	Sum of Squares	Freedom	F Value	Significant Level $p$
Model	$1.308 \times 10^5$	6	165.05	<0.0001 **	2655.25	6	15.41	0.0002 **
$X_1$	93,096.13	1	704.71	<0.0001 **	364.50	1	12.69	0.0052 *
$X_2$	31,000.50	1	234.66	<0.0001 **	1830.13	1	63.72	<0.0001 **
$X_3$	2485.13	1	18.81	0.0015 *	91.13	1	3.17	0.1052
$X_1X_2$	1936.00	1	14.65	0.0033 *	2.25	1	0.078	0.7853
$X_1X_3$	2.25	1	0.017	0.8988	6.25	1	0.22	0.6509
$X_2X_3$	2304.00	1	17.44	0.0019 *	361.00	1	12.57	0.0053 *
Residual	1321.06	10			287.22	10		
Lack of Fit	1119.86	6	3.71	0.1125	108.42	6	0.40	0.8458
Pure Error	201.20	4			178.80	4		
Cor Total	$1.321 \times 10^5$	16			2942.47	16		

\*\*  $p < 0.001$ , highly significant; \*  $p < 0.05$ , significant.

On the angle of the main effect,  $X_1$ ,  $X_2$  and  $X_3$  had highly significant effects on  $Y_1$ , while  $X_1$  and  $X_2$  significantly affected  $Y_2$ . On the angle of the interaction effects, the interactive factor  $X_1X_2$  performed a highly significant effect on  $Y_1$ , and  $X_2X_3$  displayed a highly significant effect on  $Y_1$  and  $Y_2$ . However,  $X_1X_3$  displayed no significant effect on  $Y_1$  and  $Y_2$ . Consequently, the 2FI regression models were optimized to remove the insignificant items on the conditions if  $p < 0.01$  for the model and  $p > 0.05$  for the lack of fit (Equations (8) and (9)).

$$Y_1 = 520.76 + 107.87X_1 - 62.25X_2 - 17.63X_3 - 22X_1X_2 - 24X_2X_3 \quad (8)$$

$$Y_2 = 175.18 - 6.75X_1 - 15.13X_2 - 9.5X_2X_3 \quad (9)$$

### 3.2. Influences of the Interactive Factors on Indexes

Based on the significance analysis results (Table 4), this study separately analyzed the influences of the interactive factors  $X_1X_2$ ,  $X_1X_3$  and  $X_2X_3$  on  $Y_1$  and  $Y_2$ . The interaction of  $X_1$  and  $X_2$  on  $Y_1$  with  $X_3 = 15$  mm is shown in Figure 4a.  $X_1$  and  $X_2$  were all positively correlated with  $Y_1$ . Increasing  $X_1$  and reducing  $X_2$  was conducive to improving  $Y_1$ . The reason is that the initial airflow of high-pressure airflow increased as  $X_1$  increased, and the airflow was compressed with the decreasing of  $X_2$ , which resulted in an improvement in  $Y_1$ . The interaction of  $X_2$  and  $X_3$  on  $Y_1$  with  $X_1 = 500$  kPa is shown in Figure 4b.  $Y_1$  gradually increased with  $X_1$  under the same  $X_3$  level.  $X_3$  had a positive correlation with  $Y_1$  when  $X_2$  was 8–8.6 mm, but a negative correlation when  $X_2$  was 8.6–12 mm. This is because there was an optimal  $X_3$  value, so the final section of jet flow was equal to  $X_2$  [34,35], and then the optimal airflow field could be obtained. Therefore, an optimal parameter combination of  $X_1$ ,  $X_2$  and  $X_3$  maximized  $Y_1$ .

The interaction of  $X_2$  and  $X_3$  on  $Y_2$  with  $X_1 = 500$  kPa is shown in Figure 4c.  $Y_2$  decreased with the increase of  $X_2$  under the same  $X_3$  level. In addition, there was a negative correlation between  $X_3$  and  $Y_2$  as  $X_2$  was 8–9.5 mm and a positive correlation with  $X_2$  was 9.5–12 mm. Hence, an optimal parameter combination of  $X_1$ ,  $X_2$  and  $X_3$  maximized  $Y_2$ .

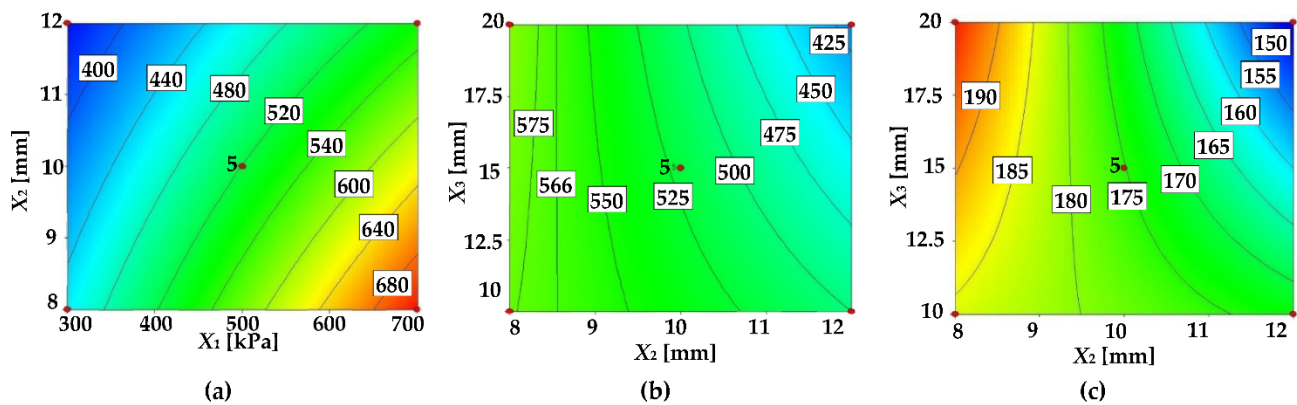


**Figure 4.** Interaction analysis of significant interactive factor. (a)  $Y_1 = f(X_1, X_2, 0)$ . (b)  $Y_1 = f(0, X_2, X_3)$ . (c)  $Y_2 = f(0, X_2, X_3)$ .

#### 4. Optimization and Verification

##### 4.1. Optimization

Combined with restraint conditions, a response-surface optimization method was applied to obtain the maximum  $Y_1$  and  $Y_2$ . The restraint condition is given as:

$$\begin{cases} \max Y_1 \\ \max Y_2 \\ 300 \leq X_1 \leq 700 \\ 8 \leq X_2 \leq 12 \\ 10 \leq X_3 \leq 20 \end{cases} \quad (10)$$

Equations (8)–(10) are solved, and the optimal parameter combination is displayed below:  $X_1$  is 686 kPa,  $X_2$  is 8 mm and  $X_3$  is 20 mm, while  $Y_1$  is  $718 \text{ m}\cdot\text{s}^{-1}$  and  $Y_2$  is 188 mm according to the 2FI regression model.

##### 4.2. Simulation Comparison

The velocity airflow field was evaluated for the PWSD with the initial combination of parameters ( $X_1 = 500 \text{ kPa}$ ,  $X_2 = 10 \text{ mm}$ ,  $X_3 = 10 \text{ mm}$ ) and the optimized combination of parameters ( $X_1 = 686 \text{ kPa}$ ,  $X_2 = 8 \text{ mm}$ ,  $X_3 = 20 \text{ mm}$ ), as shown in Figure 5. The optimized device displayed superior performance of faster and more stable airflow field in relation to the initial device in general. The initial device obtained parameters of  $Y_1$  and  $Y_2$  of  $524 \text{ m}\cdot\text{s}^{-1}$  and 176 mm, respectively, whereas the optimized device performance was  $718 \text{ m}\cdot\text{s}^{-1}$  and 188 mm, respectively (Figure 5). After improvement of the PWSD,  $Y_1$  significantly increased by 34.5% while  $Y_2$  increased by 9.1%. Furthermore, a comparative analysis between the optimized simulation results and the predicted results of the 2FI regression model shows that there is little difference because the errors of  $Y_1$  and  $Y_2$  are 1.8% and 2.1% for the initial and optimized device, indicating that a good accuracy of the model for parameter optimization.

##### 4.3. Field-Test Verification

Field-test verification of the initial and optimized devices was carried out with the pneumatic wheat-shooting principle prototype. The principle prototype comprises a rack, air compressor, air tube and PWSD, as shown in Figure 6a. We set the working pressure of the air compressor to provide continuous and stable high-pressure airflow, and the high-pressure airflow was input to the pneumatic wheat-shooting device through the air tube.



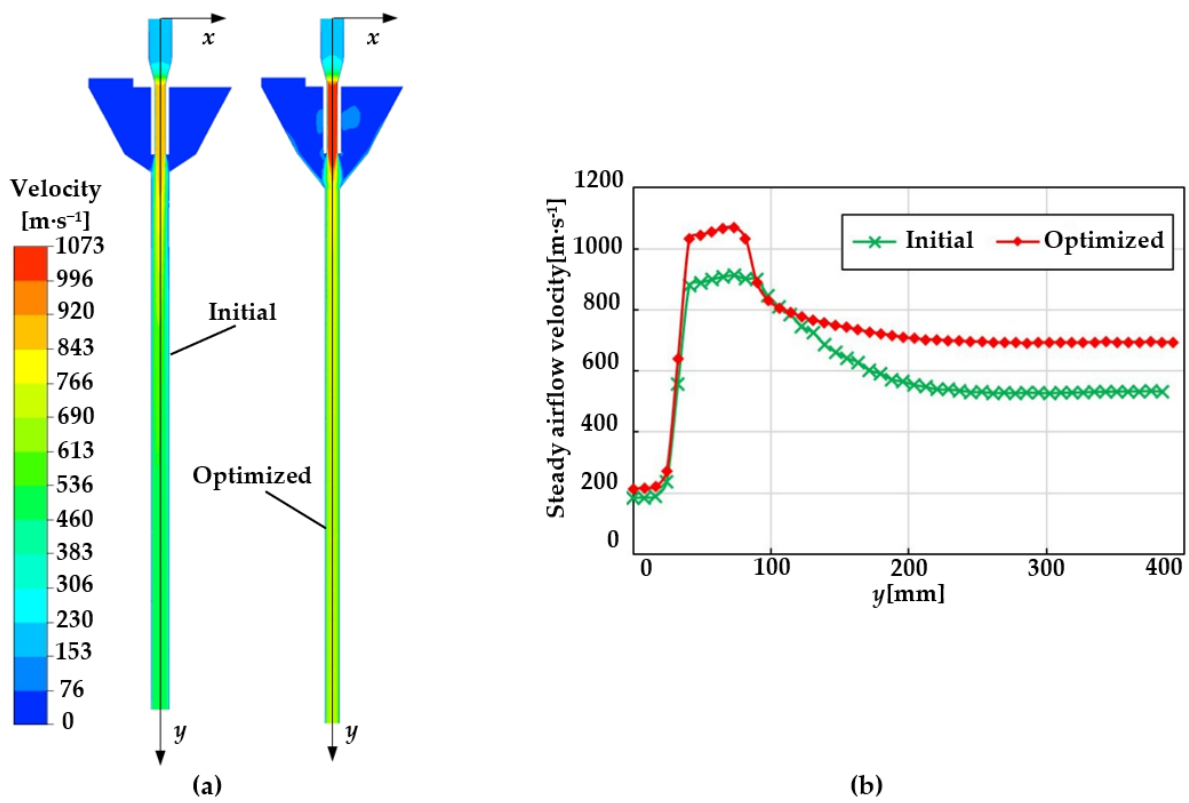


Figure 5. (a) Velocity field of initial and optimized. (b) Velocity curve of initial and optimized.

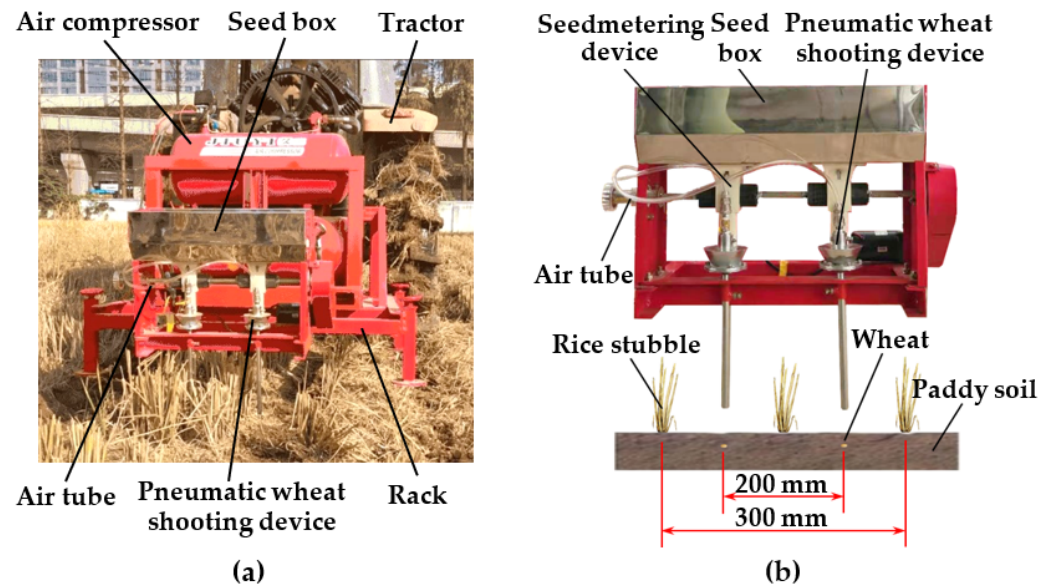


Figure 6. (a) Structure of principle prototype of pneumatic wheat-shooting. (b) Pneumatic wheat-shooting scheme in the field.

The PWSD conducts seeding on the no-till soil between the rows of rice stubble, as shown in Figure 6b. The rice-stubble height was 200–350 mm; the coverage of rice straw was about  $608 \text{ g}\cdot\text{m}^{-2}$ ; Zhengmai 9023, which is a large-scale planted variety of wheat in Hubei Province, was used for this test. Perennial rice–wheat rotation is conducted in this test plot, and the soil type is clayey paddy soil with heavy texture and high moisture content. The soil moisture content was 40.3%, and the soil compactness was 35–70 kPa within the soil depth of 0–50 mm.

#### 4.3.1. Test Method

In accordance with the China National Standard GB/T 20865-2017 “No-till and less till fertilization planter” and GB/T 6973-2005 “Testing methods of single seeding drills (precision drills)”, the pneumatic wheat-shooting test was conducted. Shooting depth was measured to reflect the operating performance of the initial and optimized device.

#### Field Seeding Depth

The vertical distance from the bottom of the wheat seed hole to the ground surface was measured with an electronic vernier caliper, and a total of 50 seeding points were counted. A total of 5 measuring sites were selected every 5 m along the working direction, and 10 seeding-depth values were randomly measured in each measuring site. The field seeding depth and stability coefficient equations can be calculated as follows:

$$\begin{cases} H_{QS} = \frac{1}{n} \sum_{i=1}^n H_{QSi} \\ S_{QS} = \frac{1}{\sqrt{n-1}} \sqrt{\sum_{i=1}^n (H_{QSi} - H_{QS})^2} \\ C_{QS} = 1 - \frac{S_{QS}}{H_{QS}} \times 100\% \end{cases} \quad (11)$$

where  $H_{QS}$  is field-seeding depth;  $H_{QSi}$  is field-seeding depth of point  $i$ ;  $S_{QS}$  is the standard deviation of field-seeding depth;  $C_{QSV}$  is the stability coefficient of the field-seeding depth.

#### Emergence Rate

Five test areas were randomly selected, and the wheat emergence rate was determined by the 5-point sampling method. The emergence rate equations can be calculated as follows:

$$C_{QSM} = \frac{1}{A_{QS}} \sum_{i=1}^n a_i \quad (12)$$

where  $C_{QSM}$  is the emergence rate;  $a_i$  is the number of wheat seedlings per row;  $n$  is the measurement number;  $A_{QS}$  is theoretical sowing rate.

#### 4.3.2. Test Results and Analysis

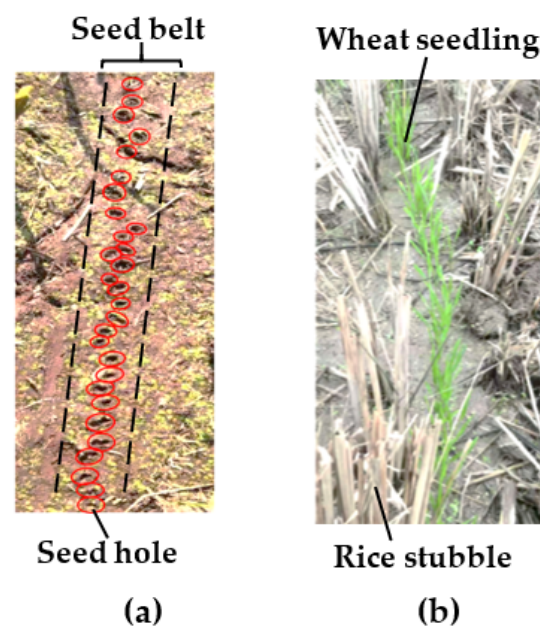
Under the field experimental conditions, the seeding operation of the pneumatic wheat-shooting principle prototype was relatively stable. The wheat was lodged into the soil and formed a single seed hole in the soil, and there was no broken strip of seed belt after pneumatic wheat shooting, as shown in Figure 7a.

Test results of pneumatic wheat seeding are shown in Table 5. The field seeding depth for the initial and optimized device was 9.96–13.12 mm and 16.24–23.74 mm, respectively. The total stability coefficients for both the initial and optimized device were more significant than 90%, which meets the requirements of Chinese national standards. The average field seeding depth of the optimized device was 19.95 mm, which was about 68% higher than the initial device, indicating that the acceleration performance of the airflow field was improved after optimization design so that wheat achieved a deeper field seeding depth with higher velocity.

Meanwhile, wheat realized a good emergence result, as shown in Figure 7b. The emergence rate for the optimized device and initial device was about 88.7% and 88.4%, respectively. The emergence rate of the optimized device was much higher than 69.8% of the traditional artificial sowing method, and there was little difference compared with 88.3% of the shallow rotary-tillage seeding technology [36,37]. The above simulation optimization design scheme and model are relatively reliable and can optimize a PWSD.

**Table 5.** Field seeding depth for initial and optimized pneumatic wheat-shooting device.

Test Item	Field Seeding Depth (mm)						
	Initial			Optimized			
	Range	Average Value	Stability Coefficient	Range	Average Value	Stability Coefficient	
Number of measurement site	1	10.56~12.84	12.02	93%	16.24~21.93	18.95	91%
	2	10.25~12.68	11.71	94%	19.31~23.74	21.07	94%
	3	9.96~12.85	11.62	92%	17.74~21.36	19.78	93%
	4	10.83~13.12	12.13	94%	18.66~21.59	20.11	95%
	5	10.48~12.93	11.73	93%	17.64~22.84	19.83	91%
Total average value		11.84			19.95		

**Figure 7.** (a) Pneumatic wheat-shooting effect in field. (b) Seeding emergence.

## 5. Conclusions

- (1) In this paper, the optimization of a PWSD was performed. There was a positive correlation between wheat velocity and airflow velocity for the pneumatic shooting process, and shooting depth was related to wheat velocity and soil properties. The shooting depth showed a positive correlation with the wheat velocity under the same soil environment. For the PWSD, the response-surface method and CFD simulation were utilized to maximize SAV and SAL, by which wheat can be sown deeper;
- (2) The central airflow velocity of the pneumatic wheat-shooting device showed a sharp increase to a maximum value, then presented a gradual decrease trend, and finally remained relatively constant by simulation analysis. The steady airflow velocity was between the maximum airflow velocity and the high-pressure airflow velocity for each experiment. The higher the high-pressure airflow velocity, the greater was the maximum airflow velocity;
- (3) Through the response-surface optimization and CFD simulation analysis, the optimal parameter combination of working pressure 686 kPa, acceleration tube diameter 8 mm and throat distance 20 mm was obtained, and the simulation result of SAV and SAL was  $718 \text{ m}\cdot\text{s}^{-1}$  and 188 mm, respectively. The optimized device had a faster and more stable airflow field than the initial one in general. After optimization, the steady airflow velocity significantly increased by 34.5%, and the SAL increased by 9.1%. The field test showed that the average field seeding depth of the optimized device was

about 68% higher than the initial device, and the emergence rate for the optimized device was about 88.7% without obvious reduction, which meets the requirements of Chinese national standards.

**Author Contributions:** Writing—original draft preparation, C.W., J.H. and H.L.; writing—review and editing, Q.W., C.L., H.Y. All authors have read and agreed to the published version of the manuscript.

**Funding:** This research was funded by the China Agriculture Research System of MOF and MARA (Grant No.CARS-03); National Natural Science Foundation of China No. 52175260.

**Institutional Review Board Statement:** Not applicable.

**Data Availability Statement:** Not applicable.

**Acknowledgments:** The authors would like to thank the Conservation Tillage Research Center for its support.

**Conflicts of Interest:** The authors declare no conflict of interest.

## References

1. China National Bureau of Statistics. Available online: <https://www.stats.gov.cn/> (accessed on 12 December 2020).
2. China Industrial Information Network. Available online: <https://www.chyxx.com/industry/> (accessed on 1 December 2020).
3. Li, C.S.; Tang, Y.L.; Xie, L.S.; Huang, G.; Zhong, G.X.; Wu, C.; Cheng, S.L. Design and experiment of 2BMFDC-6 half-tillage seeder of wheat after rice. *Southwest Chin. J. Agric. Sci.* **2011**, *24*, 789–793.
4. Sidhu, H.S.; Singh, M.; Humphreys, E.; Sidhu, B.; Dhillon, S.S.; Blackwell, J.; Bector, V.; Sidhu, M.; Singh, S. The happy seeder enables direct drilling of wheat into rice stubble. *Aust. J. Exp. Agric.* **2007**, *47*, 844–854. [\[CrossRef\]](#)
5. Zhang, X.M.; Zhang, J.M.; Xia, J.F.; Zhang, S.; Li, J.B.; Wu, H. Design and experiment on critical component of cultivator for straw returning in paddy field and dry land. *Chin. Soc. Agric. Eng.* **2015**, *31*, 10–16.
6. Tang, Y.L.; Huang, G.; Yuan, L.X. High-benefit cultivation technique of surface seeding and mulching rice straw for wheat after rice. *Crops* **2000**, *3*, 22–24.
7. Diao, P.S.; Du, R.C.; Yang, Z.D.; Yang, S.D. Theoretical research on pneumatic seeding. *J. Agric. Mech.* **2005**, *27*, 94–96.
8. Wang, Y.B.; Li, H.W.; He, J.; Wang, Q.J.; Lu, C.Y.; Liu, P.; Yang, Q.L. Parameters optimization and experiment of mechanical wheat shooting seed-metering device. *Chin. Soc. Agric. Eng.* **2020**, *36*, 1–10. [\[CrossRef\]](#)
9. Wang, Y.B.; Li, H.W.; Wang, Q.J.; He, J.; Lu, C.Y.; Liu, K.H. Design and experiment of wheat mechanical shooting seed-metering device. *Chin. Soc. Agric. Eng.* **2020**, *51*, 73–84.
10. Wang, C.; Li, H.W.; He, J.; Wang, Q.J.; Cheng, X.P.; Wei, Z.C.; Liu, J.X. Effect of incident angle on wheat soil-ripping parameters by pneumatic seeding. *Chin. Soc. Agric. Eng.* **2019**, *35*, 32–39.
11. Singh, R.C.; Singh, G.; Saraswat, D.C. Optimisation of design and operational parameters of a pneumatic seed metering device for planting cottonseeds. *Biosyst. Eng.* **2005**, *92*, 429–438. [\[CrossRef\]](#)
12. Ariaifar, K.; Buttsworth, D.; Sharifi, N.; Malpress, R. Ejector primary nozzle steam condensation: Area ratio effects and mixing layer development. *Appl. Thermal Eng.* **2014**, *71*, 519–527. [\[CrossRef\]](#)
13. Chang, J.F.; Dong, Y.P.; Liu, Q.L.; Guo, F.Q.; Zhang, T.H.; Zhang, K.W. Experimental study and numerical simulation on flow field of venturi scrubber purifying biomass gas. *Chin. Soc. Agric. Eng.* **2012**, *28*, 186–192.
14. Zhao, X.X.; Yu, H.L.; Ma, Y.J.; Zhang, J.G.; Sang, Y.Y.; Huo, X.J. Parameter optimization and experiment of negative pressure precision seed-metering device for wheat. *Chin. Soc. Agric. Eng.* **2017**, *33*, 11–18.
15. Liu, J.X.; Wang, Q.J.; Li, H.W.; He, J.; Lu, C.Y.; Wang, C. Numerical Analysis and Experiment on Pneumatic Loss Characteristic of Pinhole-tube Wheat Uniform Seeding Mechanism. *Chin. Soc. Agric. Eng.* **2020**, *51*, 29–37.
16. Cheng, X.P.; Lu, C.Y.; Meng, Z.J.; Yu, J.Y. Design and parameter optimization on wheat precision seed meter with combination of pneumatic and type hole. *Chin. Soc. Agric. Eng.* **2018**, *34*, 1–9.
17. Wang, C.; Lu, C.; Li, H.; He, J.; Cheng, X. Preliminary bench experiment study on working parameters of pneumatic seeding mechanism for wheat in rice-wheat rotation areas. *Int. J. Agric. Biol. Eng.* **2020**, *13*, 66–72. [\[CrossRef\]](#)
18. Hemidi, A.; Henry, F.; Leclaire, S.; Seynhaeve, J.M.; Bartosiewicz, Y. CFD analysis of a supersonic air ejector. part i: Experimental validation of single-phase and two-phase operation. *Appl. Thermal Eng.* **2009**, *29*, 1523–1531. [\[CrossRef\]](#)
19. Xie, J.; Liu, Y.Y.; Wang, J.F. Effects of nozzle structures of air impinging freezer on heat transfer characteristics of steel strip surface. *Chin. Soc. Agric. Eng.* **2018**, *34*, 292–298.
20. Ghalandari, M.; Kooreshahi, E.M.; Mohamadian, F.; Shamshirband, S.; Chau, K.W. Numerical simulation of nanofluid flow inside root canal. *Eng. Appl. Comput. Fluid Mech.* **2019**, *13*, 254–264. [\[CrossRef\]](#)
21. Suvarnakuta, N.; Pianthong, K.; Sriveerakul, T.; Seehanam, W. Performance analysis of a two-stage ejector in an ejector refrigeration system using computational fluid dynamics. *Eng. Appl. Comput. Fluid Mech.* **2020**, *14*, 669–682. [\[CrossRef\]](#)
22. Wang, C.; Li, H.W.; He, J.; Wang, Q.J.; Lu, C.Y.; Wang, J.X. Design and experiment of pneumatic wheat precision seed casting device in rice-wheat rotation areas. *Chin. Soc. Agric. Eng.* **2020**, *51*, 43–53.

23. Liu, Y.; Luo, C.; Zong, W.; Huang, X.; Ma, L.; Lian, G. Optimization of Clamping and Conveying Device for Sunflower Oil Combine Harvester Header. *Agriculture* **2021**, *11*, 859. [[CrossRef](#)]
24. Jin, C.Q.; Guo, F.Y.; Xu, J.S.; Li, Q.L.; Chen, M.; Li, J.J.; Yin, X. Optimization of working parameters of soybean combine harvester. *Chin. Soc. Agric. Eng.* **2019**, *35*, 10–22.
25. Hu, Y.; Chen, Y.; Wei, W.; Hu, Z.; Li, P. Optimization Design of Spray Cooling Fan Based on CFD Simulation and Field Experiment for Horticultural Crops. *Agriculture* **2021**, *11*, 566. [[CrossRef](#)]
26. Kong, F.; Kim, H.D. Analytical and computational studies on the performance of a two-stage ejector-diffuser system. *Int. J. Heat Mass Transf.* **2015**, *85*, 71–87. [[CrossRef](#)]
27. Ruangtrakoon, N.; Thongtip, T.; Aphornratana, S.; Sriveerakul, T. CFD simulation on the effect of primary nozzle geometries for a steam ejector in refrigeration cycle. *Int. J. Therm. Sci.* **2013**, *63*, 133–145. [[CrossRef](#)]
28. Wang, L.; Yan, J.; Wang, C.; Li, X. Numerical study on optimization of ejector primary nozzle geometries. *Int. J. Refrig.* **2017**, *76*, 219–229. [[CrossRef](#)]
29. Pereira, P.R.; Varga, S.; Soares, J.; Oliveira, A.C.; Lopes, A.M.; Almeida, F.G.; Carneiro, J.F. Experimental results with a variable geometry ejector using R600a as working fluid. *Int. J. Refrig.* **2014**, *46*, 77–85. [[CrossRef](#)]
30. Hewedy, N.; Hamed, M.H.; Abou-Taleb, F.S.; Ghonim, T.A. Optimal performance and geometry of supersonic ejector. *J. Fluids. Eng.* **2008**, *130*, 436–445. [[CrossRef](#)]
31. Wang, C.; Li, H.; Wang, J.; He, J.; Wang, Q.; Lu, C. CFD simulation and optimization of a pneumatic wheat seeding device. *IEEE Access* **2020**, *8*, 214007–214018. [[CrossRef](#)]
32. Ruangtrakoon, N.; Aphornratana, S. Development and performance of steam ejector refrigeration system operated in real application in Thailand. *Int. J. Refrig.* **2014**, *48*, 142–152. [[CrossRef](#)]
33. Sriveerakul, T.; Aphornratana, S.; Chunnanond, K. Performance prediction of steam ejector using computational fluid dynamic: Part 2. Flow structure of a steam ejector influenced by operating pressure and geometries. *Int. J. Therm. Sci.* **2007**, *46*, 823–833. [[CrossRef](#)]
34. Chen, W.X.; Xue, K.K.; Chen, H.Q.; Chong, D.T.; Yan, J.J. Experimental and Numerical Analysis on the Internal Flow of Supersonic Ejector Under Different Working Modes. *Heat Transf. Eng.* **2018**, *39*, 700–710. [[CrossRef](#)]
35. Arihant, S.; Abdus, S. Performance analysis of an ejector for flare gas recovery. *Geosyst. Eng.* **2014**, *17*, 169–177.
36. Li, C.; Tang, Y.; Wu, C.; Huang, G. Effect of sowing patterns on growth, development and yield formation of wheat in rice stubble land. *Chin. Soc. Agric. Eng.* **2012**, *28*, 36–43.
37. Singh, A. Evaluation of wheat sowing technologies under paddy residue conditions. *Int. J. For. Crop Improv.* **2015**, *6*, 43–48. [[CrossRef](#)]